Hybrid modeling of a miniaturized 50 W Annular Hall Thruster

Arturo Popoli, Andrea Cristofolini, Laurent Garrigues, Dongho Lee, Guentae Doh, Holak Kim, Wonho Choe

Hybrid modeling of a miniaturized 50 W Annular Hall Thruster

Arturo Popoli[*] and Andrea Cristofolini[†]
University of Bologna, Bologna, 40136, Italy

Laurent Garrigues[‡]
LAPLACE, Université de Toulouse, CNRS, Toulouse, 31062, France

Dongho Lee[§]
Georgia Institute of Technology, Atlanta, GA, 30332, USA

Guentae Doh[**]
Korea Aerospace Research Institute, Daejeon, 34133, Republic of Korea

Holak Kim[††]
Pusan National University, Busan, 46241, Republic of Korea

and
Wonho Choe[‡‡]
Korea Advanced Institute of Science and Technology, Daejeon, 34141, Republic of Korea

A 50 W-class annular Hall thruster is studied with a hybrid axial-radial 2D model. Ions are described by a kinetic approach, whereas fluid conservation equations are solved for electrons. In such models, additional (anomalous) contributions must be added to the momentum-transfer electron collision frequency to obtain realistic values of the cross-field electron mobility. First, a parametric study is performed, where anomalous transport is described with a simple two-region model based on constant empirical parameters. The simulated global performance is subsequently compared with experimental measurements. Then, laser-induced fluorescence ion velocity measurements are employed to infer a continuous profile of the anomalous electron collision frequency along the channel centerline. The model reproduces the performance, the acceleration structure, the current oscillations

[*] Tenure-track assistant professor, Department of Electrical, Electronic, and Information Engineering "Guglielmo Marconi". Corresponding author: arturo.popoli@unibo.it
[†] Professor, Department of Electrical, Electronic, and Information Engineering "Guglielmo Marconi".
[‡] Research Director, Groupe de Recherche Energétique, Plasmas et Hors Équilibre.
[§] Postdoctoral researcher, Daniel Guggenheim School of Aerospace Engineering
[**] Senior researcher, Satellite Research Directorate.
[††] Assistant professor, Department of Aerospace Engineering.
[‡‡] Professor, Department of Nuclear and Quantum Engineering.

and the doubly charged ion fraction of the laboratory thruster. Measurements of the ion velocity distribution function highlight the presence of a slow ion population in the near plume. It is shown that the production of the slow ions and their growth for increasing distances from the thruster channel exit is qualitatively reproduced by the model. The results obtained suggest that the generation and dynamics of the observed slow ions can be attributed to the presence of energetic electrons in the plume.

I. Introduction

Hall thrusters belong, along with their gridded counterparts – ion thrusters – to the broad category of electrostatic thrusters. The main idea behind this kind of device is to accelerate a stream of ions using an electric field. Ions are produced by ionization of the propellent gas, and an electric field is generated between an anode and an external cathode. The latter also serves as a source of free electrons, used to sustain the discharge, and neutralize the accelerated ions outside the thruster. A radial static magnetic field is used to increase the residence time of the electrons inside the thruster channel, allowing one to obtain remarkable ionization rates (> 90%) of the injected neutral propellent. The simultaneous presence of an electric field $\boldsymbol{E}$ in the direction of the thruster axis and a radial magnetic field $\boldsymbol{B}$ generates an electron drift in the $\boldsymbol{E} \times \boldsymbol{B}$ (azimuthal) direction, also known as the Hall current.

Thanks to the high exit velocity v_{ex} of the ions (15 to 30 km/s), the specific impulse $Isp = v_{ex}/g$ yielded by Hall thrusters can be one order of magnitude larger than that of chemical thrusters, allowing for a reduced mass of embarked propellant [1,2]. Moreover, the ion current in a Hall thruster is proportional to the neutral gas flow rate $\dot{m}$, and quasi-independent from the discharge voltage under optimal operating conditions. This allows the thruster operation to be adapted specific to tasks, making it suitable for a variety of different missions, such as orbit insertions (maximum thrust) and station keeping (maximum specific impulse) [3]. Thanks to the above described characteristics, Hall thrusters are nowadays a reliable and well established technology for space propulsion, and are employed in both short and long range missions [4–6].

In recent years, the tendency toward the employment of micro and nanosatellites has generated a corresponding technical need for small-scale and low-power plasma thrusters well suited for low-thrust missions [7,8]. However, the low-power scaling of Hall thrusters from the kilowatt range to the sub-100 W range is a challenging process from several perspectives. The increased surface-to-volume ratio over standard thrusters favor the loss of ions at the walls,

decreasing the ionization efficiency [9]. Moreover, larger flux densities (up to 400 G, as opposed to 100-200 G typical of standard-sized thrusters) are needed to achieve adequate magnetic confinement of electrons, leading to increased erosion of the channel walls [10].

Over the last decades, many efforts have been dedicated to the development of Hall thruster models. These can be subdivided into three main categories, i.e., fluid, kinetic, and hybrid models.

Fluid models such as the ones described in [11–14] require reasonable computational resources compared to the other categories, but also assume that the considered species are in (partial) thermodynamic equilibrium conditions. This might be problematic for systems where physical effects of interest occur over time scales shorter than characteristic times needed for reaching equilibrium through collision. Recently, Li et al. [15] developed a comprehensive modeling framework for HTs and proposed a modified drift-diffusion electron transport model to overcome numerical issues associated with electron transport parallel and perpendicular to magnetic field lines. Also, the well-established 2D $r-z$ Hall2De code [11] was used in conjunction with experimental measurements by Ortega, Mikellides and colleagues to perform a comprehensive evaluation of backpressure effects on the performance of an SPT-140 HT operated with a hollow cathode [16,17]. We also note the recent study by Sahu et al. [18], where the authors developed 1D full fluid moment method that they used to assess the effects on the cross-field electron transport of the quasineutral and drift-diffusion approximations often performed in computational models. Other recent interesting works involving fluid models include the 5 and 10 moment models by [19] and the Hyper2D code introduced by Boccelli et al. in [20], where a 14-moment maximum entropy method is used to provide a detailed description of ion dynamics while maintaining a reasonable computational cost.

Differently from fluid approaches, kinetic models – which can be further subdivided into direct kinetic [21,22] and particle-in-cell models [23–26] – provide a self-consistent treatment of non-equilibrium regimes; this, however, comes with demanding computational loads, which can become prohibitive for 3D and sometimes even for 2D cases. For this reason, many of the recent efforts involving fully kinetic models have been devoted to development of techniques for speeding up simulations; this can be achieved, e.g., using sparse-grid reconstruction techniques [27] or through reduced order modeling approaches such as in Reza et al. [28] where the authors developed a pseudo-2D hybrid model that showed promising results in axial-azimuthal, azimuthal-radial, and axial-radial simulations.

Lastly, we consider hybrid models, introduced during the 1990s in one dimension [29], and later extended to two-dimensional axially symmetric domains in works such as those from Komurasaki and Arakawa [30] and Fife [31].

The hybrid approach is based on the use of a particle description for ions and a fluid approach for electrons, due to their considerably faster dynamics [32–34]. Apart from a few notable exceptions [35,36], fluid-particle models are typically quasineutral, and the electric field is obtained by the electron momentum equation and current conservation. In either way, a self-consistent treatment of the ion velocity distribution function (IVDF) is obtained, without the severe performance limitations associated with full kinetic approaches [37,38]. On the other side, the macroscopic approach adopted for the electrons requires providing transport coefficients, e.g., the electron mobility for the given operating conditions. This constitutes a fundamental challenge (also for full fluid models [39]) since additional contributions to the classical cross-field electron mobility must be added to obtain realistic values for the electron current and electron mean energy [40,41].

A comprehensive review of hybrid models, together with a chronological account of modeling work up to 2018 can be found in [42]. The development and use of these codes has continued since; examples of recent efforts include [43], where Jung and Sung used a two-dimensional axisymmetric direct simulation Monte Carlo (DSMC) hybrid PIC code with a Gaussian-like anomalous collision frequency to investigate the effects of charge-exchange collisions (CEX) on a Hall thruster plasma operation and cross-field electron transport. Shashkov et al. approached the problem of fitting experimental data via the anomalous collision frequency in an axial 1D3V hybrid model using machine learning [44]. They also introduced a two- and three-dimensional velocity space axisymmetric hybrid-PIC code (Hybrid2D) that was used to study the viscosity and heat flux impact on the neutrals' dynamics and hence on the force and energy balance [45]. Panelli et al. [46] implemented a hybrid fluid-particle 2D $r-z$ code (HYPICFLU) with a two-region electron mobility model; the results of HYPICFLU were validated against the ones yielded by the HPHall-2 code by Parra et al. [47].

In this work, we use a combination of modelling (a 2D $r-z$ hybrid fluid-particle model) and experimental measurements to study the performance and the acceleration structure of a miniaturized 50 W-class annular Hall thruster (AHT). The reduced size of the thruster makes experimental measurements inside the discharge channel particularly challenging. As will be shown in later sections, simulations are also made more complex by the nonconventional operation conditions of the hollow cathode; in addition, we will show that the lower efficiency and consequent larger availability of neutrals in the near-field plume contribute to several distinctive features that are not commonly observed in standard size thrusters, e.g., the SPT-100. We start by performing a parametric study where we show that the thruster performance cannot be fully reproduced using a simple two-region anomalous electron

transport model. We then adopt a more detailed approach, where we enforce a continuous collision frequency profile along the channel centerline, based on the results of experimental measurements. In this way, the measured thrust, average discharge current and efficiency are reproduced together with the LIF-measured most probable ion velocity and plasma potential. Finally, we compare the simulated and measured current oscillations and ion velocity distribution function (IVDF) at several positions outside the thruster exhaust. The results suggest the presence of a population of energetic electrons in the near-field plume, probably due to the non-self-sustained cathode operation.

The employed numerical methodology is discussed in Section 2, emphasizing the treatment of the anomalous electron transport inside and outside the thruster channel. The characteristics of the considered laboratory thruster are described in Section 3. Then, in Section 4, the simulation results obtained with the described model are shown and compared to the experimental measurements performed on the laboratory thruster.

II.Numerical Model

A. Ions and Neutrals

As anticipated, the model employed in this work is hybrid, meaning that a different approach is used to represent electrons and heavy species (neutral and ion). Transport of neutrals and ions is computed as in [48,49], with a 2D-3V particle approach in a two-dimensional cylindrical $r-z$ domain. Computational macroparticles representing neutrals are injected into the computational domain at the anode, with a random radial position with semi-isotropic velocities determined from the species temperature. An additional flux of neutrals is also injected from the opposite end of the computational domain to account for backpressure effects. The particle trajectories are integrated at interleaved time instants with the well-established leapfrog method, and magnetic field effects on ions are disregarded to their large Larmor radius at typical HT magnetic field values. Neutral atoms hitting the walls are reflected isotropically, whereas wall recombination of ions are treated by removing the impacting ions and generating the corresponding neutrals. The generated neutrals are injected perpendicularly to the wall, with a temperature equal to the wall temperature.

Source terms for the generation of ions are given by the product of the local number densities of the species involved in the given process and reaction coefficients, following the following form:

$$S_k = n_i n_j k_{ij}(\varepsilon), \tag{1}$$

where n_i and n_j are number densities, e.g., of ground state xenon and electrons when S_k is the source term for single ions; the reaction coefficient k_{ij} for the kth process between species i and j depends on the electron mean energy and

is computed assuming a Maxwellian EEDF. We only consider single and double ions. Triple ions are disregarded since their contribution to the thruster performance is likely negligible for anode voltage levels considered in this work [50,51].

B. Electrons

Unlike ions and neutrals, electrons are described with a fluid approach. The adopted methodology, described in detail in [48], is based on solving the first three moments the Boltzmann equation under the assumption of a Maxwellian and isotropic electron energy distribution function. The number density continuity equation is expressed as:

$$\nabla \cdot \boldsymbol{\Gamma}_e = Nnk_i - \frac{\partial n}{\partial t} = \nabla \cdot \boldsymbol{\Gamma}_i, \tag{2}$$

where $\boldsymbol{\Gamma}_e$ and $\boldsymbol{\Gamma}_i$ are the electron and ion fluxes, respectively; n and N are the plasma and neutral atoms number densities, respectively; k_i is the ionization rate, which depends on the mean electron energy ϵ. The plasma density in Eq. (2) is directly obtained from the ion density computed with the kinetic approach, under the hypothesis of quasi-neutrality. Given that both single and double ions are considered, one has $n = n_{i^+} + 2n_{i^{2+}}$. Neglecting the electron inertia (which is equivalent to a low-Mach number approximation in fluid dynamics [51]), the electron momentum continuity equation can be expressed in drift-diffusion form as:

$$\boldsymbol{\Gamma}_\mathrm{e} = -n\bar{\boldsymbol{\mu}} \cdot \boldsymbol{E} - \frac{2}{3e}\bar{\boldsymbol{\mu}} \cdot \nabla(n\epsilon), \tag{3}$$

where $\bar{\mu}$ and $\boldsymbol{E}$ represent the electron mobility tensor and the electric field, respectively. Finally, the electron energy conservation is:

$$\frac{\partial(n\epsilon)}{\partial t} + \frac{5}{3}\nabla \cdot (\boldsymbol{\Gamma}_e\epsilon) + \nabla \cdot \boldsymbol{q}_e = -e\boldsymbol{E} \cdot \boldsymbol{\Gamma}_e - P_{col} - P_w, \tag{4}$$

where $\boldsymbol{q}_e = -\frac{10}{9}n\epsilon\bar{\boldsymbol{\mu}} \cdot \nabla\epsilon$ [31] is the conduction heat flux, assumed proportional to the temperature gradient; in the right-hand side of Eq. (4), the first term represents electron energy density gains due to the electric field. P_{col} represents energy losses due to inelastic collisions between electrons and ions: $P_{col} = Nn\kappa^0 + n_{i^+}n\kappa_\epsilon^I$. κ^0 is the effective rate for inelastic energetic losses to ground-state neutrals (including direct ionization), while κ_ϵ^I is the effective rate for stepwise ionization. All effective loss rates are computed assuming a Maxwellian EEDF [52], where

the Maxwellian temperature T_e is defined as $T_e = \frac{2}{3}\frac{\epsilon}{k_B}$; The term $P_w = nW$ represents energetic losses due to wall collisions; The W coefficient is discussed in the next section.

The electron dynamics are solved under the assumption that the electrons – trapped by the radial field provided by the magnetic circuit – are in thermodynamic equilibrium along each magnetic field line. Given the magnetic vector potential distribution $\boldsymbol{A}_\theta$, computed using the free software FEMM [53], a scalar magnetic stream function λ can be defined such that λ is constant along the magnetic field lines ($\boldsymbol{B} \cdot \nabla\lambda = 0$) and increases monotonically from the thruster anode to the cathode. In this way, a quasi-1D grid such as the one shown in Fig. 1 is defined. The electron dynamics in the directions parallel and perpendicular to the magnetic field can be treated separately. Indeed, the gradient of a generic quantity perpendicular to the magnetic field lines can be expressed as [31]:

$$\nabla_\perp(\cdot) = rB\frac{\partial}{\partial\lambda}. \tag{5}$$

In this way, spatial derivatives in the direction parallel to the electric field can be expressed as derivatives with respect to λ, which is constant along each magnetic field line. The electron energy is uniform along each magnetic field line, i.e., $\epsilon = \epsilon(\lambda)$. Since the electric force and the pressure gradient are assumed to be in equilibrium, one has from Eq. (3) that:

$$n\nabla_\parallel\phi = \frac{2}{3e}\nabla_\parallel(n\epsilon). \tag{6}$$

The integration of Eq. (6) along a field line (where ε is constant) using the property in Eq. (5) allows to express the local electric potential ϕ as a function of the local plasma density n, the electron mean energy $\epsilon(\lambda)$ and a *thermalized* electric potential $\phi^*(\lambda)$:

$$\phi = \phi^*(\lambda) + \frac{2}{3e}\epsilon(\lambda)\ln\left(\frac{n}{n_0}\right). \tag{7}$$

The quantities $\epsilon(\lambda)$ and $\phi^*(\lambda)$ in Eq. (7) are uniform along magnetic field lines, and n_0 a reference plasma density. As anticipated, the model is quasi-neutral: this alleviates the typical requirement of non-neutral models on the local mesh size being smaller than the Debye length; also, it prevents one from using Poisson's equation to compute the electric potential. Perpendicularly to the magnetic field Eq. (3) can be rewritten using Eqns. (5) and (7):

$$\Gamma_{e,\perp} = rB\mu_\perp n\frac{\partial\phi^*}{\partial\lambda} + \frac{2}{3e}rB\mu_\perp n\left(\ln\frac{n}{n_0} - 1\right)\frac{\partial\varepsilon}{\partial\lambda}, \tag{8}$$

where $\mu_\perp$ represents the cross-field electron mobility. Then, using the current conservation to substitute $\Gamma_{e,\perp}$ and integrating over the surfaces defined by magnetic field lines, one gets a one-dimensional problem across the magnetic field lines replacing the continuity and momentum equations (2) and (3):

$$\int_S \Gamma_{i,\perp}\, dS - \frac{1}{e} I_d = \int_S rB\mu_\perp n \frac{\partial \phi^*}{\partial \lambda} dS + \int_S \frac{2}{3e} rB\mu_\perp n \left(\ln\frac{n}{n_0} - 1\right)\frac{\partial \varepsilon}{\partial \lambda} dS, \tag{9}$$

where $\Gamma_{i,\perp}$ is the ion flux, determined from the particle model, and I_d is the discharge current. The obtained equation and Eq. (4), which is treated similarly, yield ϕ^* and ε at the given time-step. The two quantities are then used in in Eq. (7) to find the electric potential. Details on the discretization process and numerical solutions of the above expressions can also be found in [48]. Considering again Fig. 1, the boundary conditions for the electron energy equation are set by fixing the electron mean energy along the two magnetic field lines intersecting the anode and the cathode, marked in red; the fluid equations are solved between the k −th and the $k+1$ −th magnetic field lines; the channel exit is marked with $z = 0$. Beyond the anodic and cathodic boundaries, the electron energy is fixed at the same value used for the anodic/cathodic field lines and the term $\frac{1}{e} I_d$ is set to zero in Eq. 9.

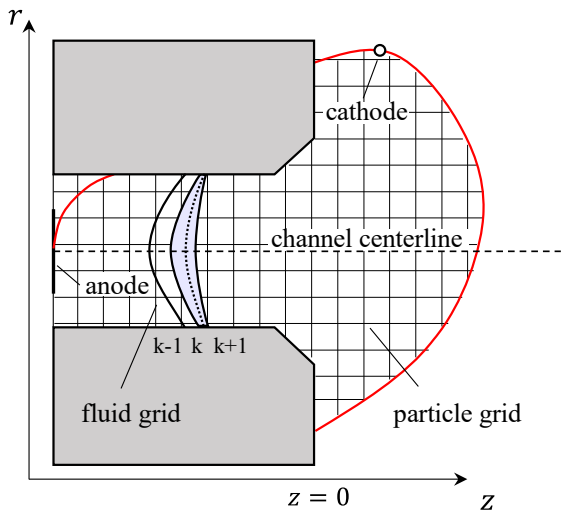

Fig. 1: Sketch of the cartesian 2D r-z for the particle modeling of the heavy species and the quasi-1D grid for the fluid modeling of electrons.

Anomalous Transport

The adoption of a fluid approach for the physical description of the electrons grants substantial advantage in terms of computational performance. Indeed, the time-step required for the stability of the macroparticle trajectories integration is no longer limited by the fast dynamics of the electrons, with substantial benefits in terms of

computational effort. However, appropriate expressions for the collisional phenomena appearing in the electron momentum and energy Eqs. (3) and (4) must be provided. Accurate modeling of the electron transport in the direction perpendicular to the magnetic field is a challenging task when fluid models are employed. The classical expression for the cross-field electron mobility is [54]:

$$\mu_{\perp} = \frac{e}{m_e} \frac{\nu}{\nu^2 + \Omega_{ce}^2} \approx \frac{m_e}{eB^2} \nu, \tag{10}$$

where e, m_e and $\Omega_{ce} = eB/m_e$ are the electron charge, mass and cyclotron frequency, respectively, and $\Omega_{ce} \gg \nu$; the total electron momentum exchange collision frequency $\nu = \nu_{e-N} + \nu_C$ is constituted by electron-neutral (ν_{e-N}) and Coulomb (ν_C) collision frequencies. Unfortunately, as anticipated, the cross-field mobility in Eq. (10) does not produce results compatible with experimental measurements: discrepancies between simulations and experiments are found in the computed electron energy and in the electron contribution to the discharge current. For the above reasons, an effective electron collision frequency accounting for additional physical effects in the presented methodology is defined as:

$$\nu = \nu_{e-N} + \nu_C + \underbrace{\nu_w + \nu_B}_{\nu_{an}}, \tag{11}$$

where the ν_w and ν_B are the above-mentioned additional terms used to represent the effects of anomalous transport inside and outside the thruster channel, respectively ($\nu_{an} = \nu_w + \nu_B$). Inside the channel, momentum transfer collisions between electrons and thruster walls are one of the main mechanisms responsible for anomalous transport [55–57]. Sufficiently energetic electrons cross the potential barrier created by the sheaths, colliding against walls, and possibly generating secondary electrons. Conversely, outside the thruster channel the experimentally observed anomalous transport phenomena are usually attributed to field fluctuations and are usually modelled as a Bohm-like diffusion [42]. From a numerical point of view, two different strategies to account for the anomalous collision terms (and their associated mobilities) in Eq. (11) are implemented in the model. The first approach consists of writing the terms responsible for anomalous transport (ν_w and ν_B) as a function of constant empirical parameters. In this case the wall collision frequency inside the thruster channel is estimated with the following expression:

$$\nu_w = \alpha \nu_{ref}, \tag{12}$$

where α is a constant coefficient, multiplying a reference collision frequency ν_{ref}. In this work, $\nu_{ref} = 10^7$ s^{-1}.

where B represents the magnetic field magnitude. The range of realistic values for the empirical coefficient α is discussed in the following section. Outside the thruster channel, the effective collision frequency associated with Bohm diffusion can be written as a function of B, the electron mass m_e and an empirical coefficient k_B:

$$\nu_B = \frac{eB}{m_e}\frac{k_B}{16}. \tag{13}$$

The total cross-field electron mobility including the additional contributions to momentum-exchange collisions is then:

$$\mu_\perp = \frac{m_e}{eB^2}(\nu_{e-N} + \nu_C + \nu_w + \nu_B) \tag{14}$$

As an alternative to the discussed two-region approach based on using constant values of α and k_B, a continuous anomalous collision frequency distribution can also be manually enforced. This can be useful when experimental data on the considered thruster are available, allowing us to adjust the anomalous frequency distribution to match the measured physical quantities of interest. In Section III, both strategies are employed to simulate the considered 50 W-class AHT.

C. Sheath model

As previously mentioned, the coefficient W in Eq. (4) represents effective energy loss per unit time coefficient due to electron-wall interactions. A simple way to compute W is via an empirical formula, such as $W = \alpha_\epsilon \nu_{ref} \epsilon \exp(-U/\epsilon)$, where the parameter α_ϵ and the energy threshold U are adjusted to match experimental results. This method was as used in previous works on full size thrusters such as [49]. In order to provide a more self-consistent approach, the semi-analytical electron-sheath interaction model developed in [58] is used in this work.

For a Maxwellian electron energy distribution function, the effective energy loss per unit time coefficient can be obtained from the balance between electron energy flux to and from a generic wall element [58]. The electron energy flux can be related to the ion flux – known at each time-step from the kinetic solution of the ion dynamics – giving:

$$W = \frac{\iint_s \Gamma_{i,w}\, dS}{\iiint_V n\, dV}\left[\frac{4(\epsilon - \overline{\gamma}\epsilon_s)}{3(1-\overline{\gamma})} + \Delta\phi_s\right], \tag{15}$$

where $\iint_s \Gamma_{i,w}\, dS$ is the number of ions colliding with a wall element between two consecutive magnetic field lines per unit time, and $\iiint_V n\, dV$ is the number of ions (and electrons) in the volume between the two considered lines; $\overline{\gamma}$ is the effective total secondary electron emission (SEE) yield. This is obtained over a Maxwellian EEDF the total

secondary emission yield $\gamma(\epsilon) = \gamma_0 + \epsilon/\epsilon^*(1-\gamma_0)$, where ϵ^* is a crossover energy and γ_0 is the yield for $\epsilon = 0$. While the expression for $\gamma(\epsilon)$ is general, these two parameters depend on the specific dielectric material. The term ϵ_s in Eq. (15) is the electron mean energy of wall-emitted electrons [59]; $\Delta\phi_s$ is the sheath potential drop, obtained from the zero-current condition at dielectric walls $\Gamma_{i,w} = \Gamma_{e,w}(1-\overline{\gamma})$ and the assumption of a linear dependence of the SEE yield from the electron mean energy [59]:

$$\Delta\phi_s = \frac{2}{3}\epsilon \ln\left[(1-\overline{\gamma})\sqrt{\frac{m_i}{2\pi m_e}}\right]. \tag{16}$$

Ions at the sheath entrance and force their radial mean velocity to be consistent with the kinetic Bohm criterion for single and double ions derived in [60]. Practically, this is done by isolating ions located in a strip of thickness d_w close to the walls (typically $d_w \sim 150$ μm). The wall-normal component of the selected ions velocity is then incremented by an amount such that that the ion mean velocity equals the Bohm velocity. Thanks to this correction, the pre-sheath profile establishes itself in just a few iterations. After that, the velocity correction that needs to be applied is substantially lower. In the acceleration region, where sufficient kinetic energies are reached, ion bombardment of walls causes erosion due to sputtering. This is considered in the model by discretizing the channel walls into elements with the same length as the local grid size. For each wall element, the erosion rate due to sputtering Ω_w is computed with an empirical expression:

$$\Omega_w = \frac{\Gamma_{i,w} m_w}{\rho_w} Y\left(\epsilon_{i,w}, \theta_{i,w}\right), \tag{17}$$

where $\Gamma_{i,w}$ is the total ion flux at the considered wall element; m_w, ρ_w and Y are the mean wall particle mass, the wall density and the wall sputtering yield (which depends on the incident ion energy and mass), respectively. The kinetic energy of wall-directed ions (acquired in the quasineutral region) is increased by an amount corresponding to the sheath potential drop $\Delta\phi_s$ in Eq. (16). When a steady-state regime is achieved for Ω_w the simulation is stopped, and the channel shape is modified using the computed erosion rate.

III.Thruster Description

The considered 50 W-class AHT, depicted in Fig. 2, is equipped with ceramic chamfered walls and exhibits two different discharge modes (A and B) depending on the given anode voltage and the Xe flow rate. Mode A operation is achieved when low flow rates are employed ($\dot{m} < 0.37$ mg/s), or low anode voltages ($V < 200$ V) with higher flow rates. Compared to mode B (0.42 mg/s, 200 V), mode A (0.42 mg/s, 160 V) is associated with lower values of thrust

(3.3 mN versus 3.8 mN), higher values of plume divergence (68º versus 52º) and discharge current (0.36 A versus 0.30 A).

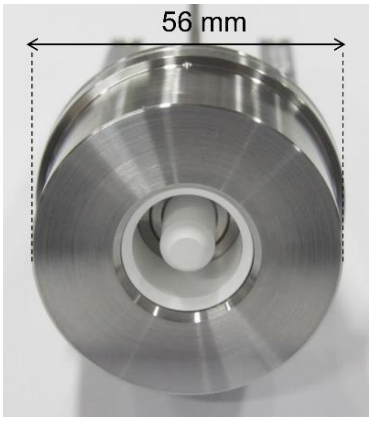

Fig. 2: 50 W-class miniaturized AHT, developed at the Korea Advanced Institute of Science and Technology (KAIST) [61].

Specifically, the observed discharge current increase is mainly due to the electron current component (+30%), while the ion current increase is only +4%. Hence, when the thruster is operated in mode A, significantly lower values of anode efficiency are obtained. In addition, higher fractions of multiply charged Xe ions are observed in mode A with respect to mode B. Laser-induced fluorescence (LIF) measurements of the ion velocity in the plume have shown that the acceleration of the Xe ions outside the channel exit takes place in a considerably longer region when the thruster is operated in mode A. The simulation process described in this work is limited to the analysis of mode B, which yields the best global thruster performance. A detailed discussion on the two distinct operating modes can be found in [61]. In order to provide a reference point for the simulation results, several macroscopic performances of the thruster have been selected from the experimental data to be compared with the ones yielded by the employed hybrid model. These include the discharge current (given by the sum of the ion and electron currents, $I_d = I_e + I_i$), the thrust, the specific impulse and the anode efficiency. The thrust obtained depends on the propellant mass and exit speed. These two quantities can be approximated by $\dot{m}_i$ and v_i due to the large velocity of the ions greatly exceeding that of the neutral gas propellant:

$$T = \dot{m} v_{ex} \approx \dot{m}_i v_i, \tag{18}$$

while the anode efficiency is given by the ratio of the power imparted to the expelled jet and the electric power P_{el} provided to the thruster:

$$\eta = \frac{T^2}{2\dot{m}P_{el}}. \tag{19}$$

In Eq. (19) the electric power is computed as the product of the anode voltage V and the discharge current I_d, hence neglecting the power consumption of the cathode and the magnetic circuit (if powered coils are employed instead of permanent magnets).

Finally, the strength and field lines of the magnetic field in proximity to the channel exit are shown in Fig. 3 for the considered thruster. In this study, LIF spectroscopy was used to measure the axial profiles of time-averaged ion velocity distributions in this micro-Hall thruster. Using the same experimental setups described in Ref. [62,63], the tunable laser beam was injected along the mid-channel axis to excite the metastable $5d^2F_{7/2}$ state to the $6p^2D^0_{5/2}$ state. An excitation by the incident wavelength of 834.72 nm was used while a fluorescence signal of 541.9 nm was measured, which was discriminated from the background Xe II emission by using a lock-in-amplifier. The collecting optics, which acquires the fluorescence signals emitted from the subsequent transition to the state $6s^2P_{3/2}$ was installed with an angle of 58° with respect to the incident beam axis. Then, time-averaged ion velocity distribution functions were obtained at different axial locations by moving the thruster along the axial direction using a linear stage.

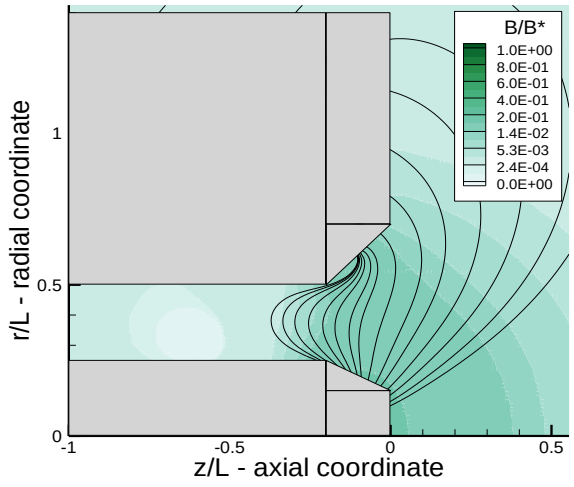

Fig. 3: Magnetic field magnitude (normalized) and magnetic field lines near the channel exit.

IV.Results and Discussion

This section deals with the simulation of the considered 50 W-class AHT, when operated under the conditions described in Section 3. First, a description of the boundary conditions and main setting used in the two-dimensional

hybrid code is provided in Section 4.1. Then, in the following sections, two different approaches are adopted for the description of the anomalous cross-field electron transport. A parametric analysis of thruster performance is carried out in Section 4.2 over a range of the empirical parameters α and k_B. These, as described in Eqs. (12) and (13), regulate the anomalous collision frequency inside (ν_W) and outside (ν_B) the discharge channel, respectively. Then, in Section 4.3, the measured discharge current and the most probable ion velocity are used to infer a continuous profile of anomalous electron collision frequency that allows reproducing the global performance and acceleration structure of the thruster. The obtained results are compared to the ones yielded by the parametric analysis carried out in Section 4.2 and to the measurements performed on the laboratory thruster.

D. Simulation Settings

In all the simulations described in the following sections, Xe atoms are injected from the anode at a constant flow rate (0.42 mg/s), at a temperature of 500 K. The backpressure due to the vacuum chamber is set to 1 mPa. Regarding the boundary conditions for Eq. (4), the electron mean energy ϵ has been enforced along the anodic ($\epsilon_a = 2$ eV) and cathodic ($\epsilon_c = 7.5$ eV) magnetic field lines (see Fig. 1 for visual reference). Since electrons are practically unmagnetized near the anode, the results are weakly affected by ϵ_a. The value for ϵ_c has been selected according to the electron mean energy measurements performed in [61].

Applied Voltage

While the laboratory thruster is operated with a 200 V anode voltage (V_{anode} in the following), a lower anode voltage level ($V_{anode,sim}$) is used in the simulations to account for the measured plasma potential distribution. A qualitative representation of this quantity along the channel centerline is given in Fig. 4(a). As expected, the electric potential quickly drops across the exhaust region because of the strong local magnetic field, reducing the local plasma conductivity. However, the potential drop starts to slow down after the exhaust, and the electric potential gradually decreases until reaching the end of the discharge chamber (grounded). This observed local electric potential behavior in the near-field plume can probably be attributed to the operation of the hollow cathode shown in Fig. 4(b). In fact, the keeper voltage source has been kept active during the thruster laboratory operation of the thruster, with $V_{\mathrm{keeper}} \sim 50$ V (also marked in Fig. 4(a)). Note that this regime is not uncommon for low-current thrusters, where often cathodes cannot achieve stable operation and operate in self-sustained mode [64–66]. As a result, the beam voltage in the near-field plume is considerably reduced with respect to standard AHTs, where it usually ranges between 90 % to 95 % of

the discharge voltage [2]. Following the mid-channel line, the computational domain ends 22 mm downstream of the channel exit. We refer to this position as z_{end} in the following. The measured local electric potential at z_{end} is $\phi_{meas}(z_{end}) = 59$ V. Therefore, the anode voltage has been set to $V_{anode,sim} = \phi_{anode} - \phi_{meas}(z_{end}) = 141$ V in the simulations, to ensure that the ion beam is subject to the same voltage drop between experiments and simulations.

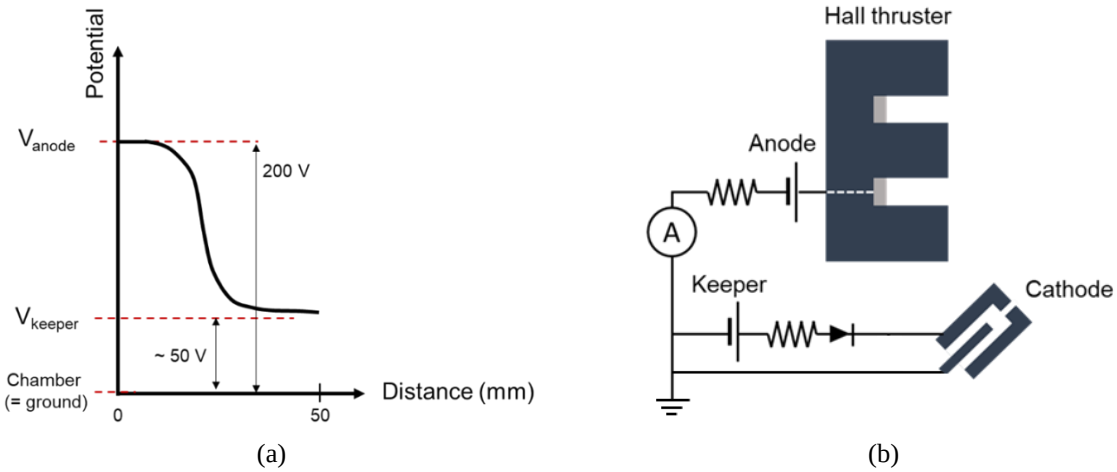

(a) (b)

Fig. 4: (a) Sketch of the electric potential profile along the channel centerline of the laboratory thruster for increasing distances from the anode; (b) simplified electrical schematic.

Correction factor

The computational domain ends downstream of the channel exit ($z_{end} = 22$ mm). In the laboratory thruster, the electric potential gradually decreases downstream of z_{end}, i.e., outside the part of the plume captured in the computational domain. This is suggested by 1) the low electric potential slope measured in the near-field plume in [61] and 2) the ion beam energy (~ 180 eV) measured 480 mm from the anode by a retarding potential analyzer (RPA). This means that the ion beam is further accelerated over a long axial distance after the end of the computational domain. Since this feature cannot be directly captured within the model, a correction factor k_c is defined for the computed thrust and specific impulse. If the region downstream of z_{end} is collisionless, the correction factor k_c is defined as:

$$k_c = \sqrt{\frac{V_{anode}}{V_{anode,sim}}}. \tag{20}$$

In this way, the modified thrust and the specific impulse read as $T^* = k_c T$ and $Isp^* = k_c Isp$, respectively. Note that the anode efficiency defined in Eq. (19) must be updated accordingly as well:

$$\eta^* = \frac{(k_c T)^2}{2\dot{m}(k_c^2 V_{anode,sim}) I_d} = \frac{T^{*2}}{2\dot{m} V_{anode} I_d}. \quad (21)$$

The asterisk superscript in T^*, Isp^* and η^* will be omitted here onwards for the sake of conciseness.

Grid and macroparticles number dependence

In this paragraph we present an analysis that was performed to select the grid density and the number of macro-particles used to represent ions in the simulations. The computational grid is structured; within the channel, a uniform spacing is used along both the axial and radial directions. Conversely, the grid spacing increases with the axial coordinate z downstream of the channel exit. Along the radial direction, the grid spacing increases with the radial coordinate r outside the channel. Here we focus on selecting suitable values for three quantities: the number of cells inside the channel along the axial and radial direction (n_{gax}, n_{gr}) and the number of macro-particles representing ions (n_{mp}) within the computational grid. Differently from neutrals (modeled with a constant statistical weight), for ions the same number of macro-particles is injected at each time-instant. The specific weight (the same for all ions injected at one instant) is adjusted over time to follow the local kinetic source term.

The quantity n_{mp} changes significantly during the discharge ignition and during oscillations, and we will therefore refer to its value when stable thruster operation is reached. The analysis is performed with a two-region anomalous conductivity model, where $\alpha = 1.8$ and $k_B = 0.67$. We refer the reader to the next section for more details on the model. Figure 5 shows the obtained thrust for a sweep of n_{gax}, n_{gr} and n_{mp}. When n_{gax} is changed, $n_{gr} = 60$ and $n_{mp} = 1.65 \cdot 10^5$; when n_{gr} is changed, $n_{gax} = 50$ and $n_{mp} = 1.65 \cdot 10^5$; the sweep of n_{mp} is performed using $n_{gax} = 50$ and $n_{gr} = 60$. The results show that small thrust variations are obtained when $n_{gax} > 30$, $n_{gr} > 40$ and $n_{mp} > 1.05 \cdot 10^5$. Based on the results in Fig. 5, the simulations in the following sections are all performed using $n_{gax} = 50$ and $n_{gr} = 60$ and $n_{mp} = 1.65 \cdot 10^5$.

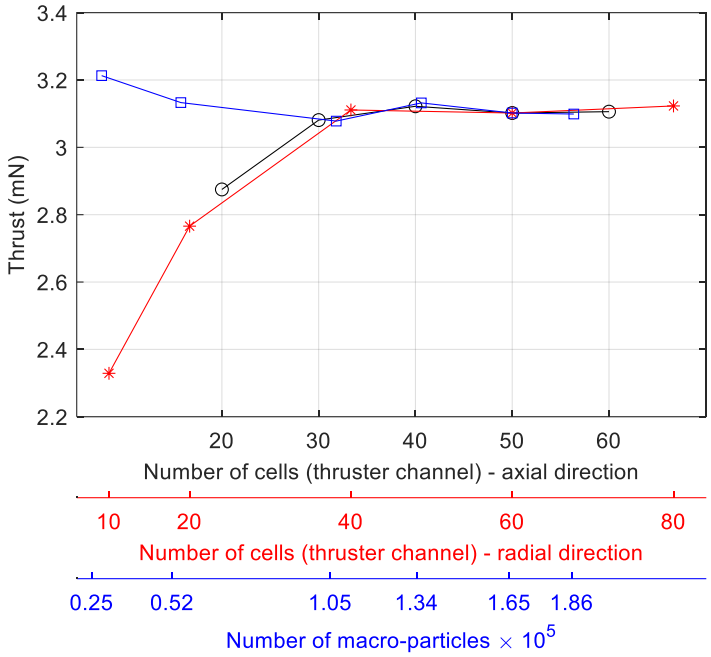

Fig. 5: Dependence of the computed thrust on the number of cells within the thruster channel and on the total number of macroparticles in the computational domain.

E. Constant Empirical Parameters Approach – Parametric Simulation

As anticipated, the parameter α in Eq. (12) determines the wall collision frequency ν_w, which accounts for electron momentum losses inside the thruster channel. This coefficient was found to be realistic in the range $[0.1 - 1]$ in a previous study on the SPT-100 thruster [49]. For the present parametric analysis, the range of α is extended to $[0.2 - 4]$ to account for the channel size reduction in the considered miniaturized AHT. Outside the channel exit, the anomalous collision frequency ν_B depends on the coefficient k_B, as expressed in Eq. (13). k_B is varied within the range $[0.05 - 1]$, where $k_B = 1$ yields a full Bohm mobility, see Eq. (13). Both intervals for α and k_B are subdivided in 15 evenly spaced points, corresponding to 225 simulations. The computed thrust T, discharge current I_d and anode efficiency η as a function of the enforced values for α and k_B are shown in Fig. 6(a), Fig. 6(b) and Fig. 6(c), respectively. Focusing on Fig. 6(a), Fig. 6(b), most of the T and I_d growth is obtained when α and k_B are increased to roughly 1/2 and 1/4 of their respective ranges. Above these values, i.e., when $\alpha > 2$ and $k_B > 0.25$, the thruster performance dependence on the empirical transport parameters decreases significantly.

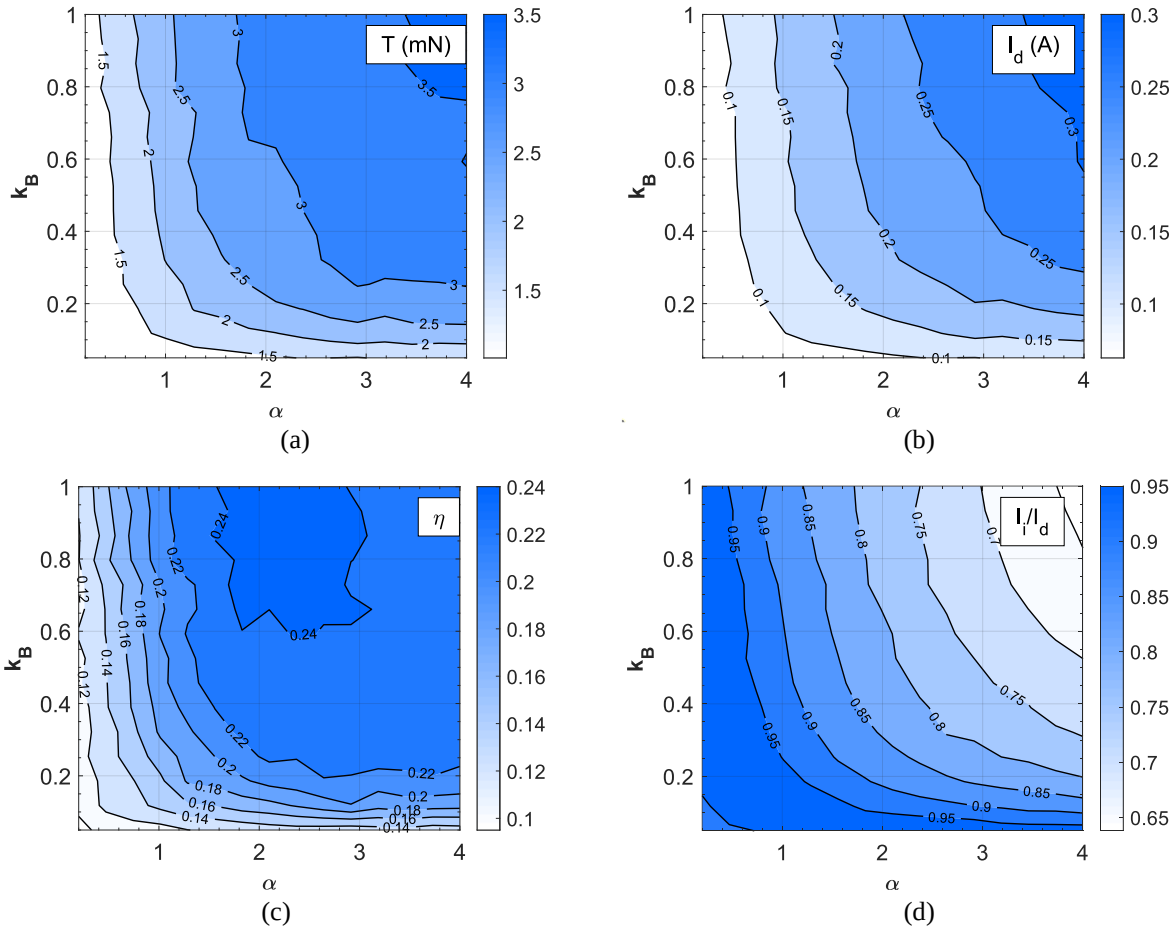

Fig. 6: Dependence of computed thrust (a), discharge current (b), anode efficiency (c) and ratio between the ion and electron current (d) on α and k_B.

This observation is consistent with the results obtained in previous studies performed on the larger SPT-100 geometry [49], and shows that – once a sufficiently high cross field electron transport is reached – the thruster macroscopic performance is mainly established by the geometry, the magnetic topology and the given operational conditions (such as flow rate and anode voltage). Compared to T and I_d, the anode efficiency η in Fig. 6(c) exhibits a different behavior when α (anomalous transport inside the channel) is increased. Indeed, η starts to progressively decrease for $\alpha \geq 3$, because the growth electron current (I_e) caused by the enhanced transport inside the channel is not accompanied by a corresponding increase of ion current (I_i), leading to the observed lower efficiency. The described behavior of the two current components (evaluated at the cathode field line) can be seen in Fig. 6(d), where the ratio between the ion current and the total discharge current (I_i/I_d) decreases for increasing values of the electron anomalous transport inside and outside the thruster channel.

To evaluate the agreement between the measured performances and the parametric simulation results, a relative error ε_{rel} has been defined using the difference between the computed and measured thrust (T), discharge current (I_d) and anode efficiency (η):

$$\varepsilon_{rel} = \Delta T + \Delta I_d + \Delta \eta, \tag{22}$$

where, for example,

$$\Delta I_d = \frac{|I_{d,meas} - I_d|}{I_{d,meas}}. \tag{23}$$

In the previous expression, $I_{d,meas}$ and I_d are the measured and computed values of discharge current, respectively. Among the results of the parametric simulation in Fig. 6, the minimum value for ε_{rel}, i.e., $\varepsilon_{rel,m} = \min(\varepsilon_{rel})$ is obtained by setting $\alpha = 3.46, k_B = 0.86$.

The macroscopic thruster performance yielded by these values for α and k_B is compared to the experimental measurements ($V_{anode} = 200$ V, $\dot{m} = 0.42$ mg/s) in Table 1. The simulation results in the column *Simulation* – α, k_B correspond to the ones obtained with the described two-region model using $\alpha = 3.46, k_B = 0.86$. The results in the column *Simulation – continuous* ν are be discussed in the next section.

Table 1: Measured and simulated thruster performance using two anomalous electron transport models: a two-region model and the continuous collision frequency profile (continuous ν_{an}) in Fig. 8(b).

Quantity	**Measurement**	**Simulation** – α, k_B	**Simulation** – **continuous** ν_{an}	**Units**
Anode power $-$ P_{el}	60.8	60.31	61.20	W
Discharge current $-$ I_d	0.30	0.30	0.31	A
Thrust $-$ T	3.8	3.52	3.80	mN
Specific Impulse $-$ Isp	913	854	921	s
Anode Efficiency $-$ η	0.28	0.24	0.28	-

The computed discharge current I_d is identical to the measured value. The thrust T and the specific impulse Isp are about ~ 93 % of the measurements. The obtained anode efficiency η is ~ 86 % of the measured value. The terms of the total momentum-transfer collision frequency ν in Eq. (11) are plotted for the selected case ($\varepsilon_{rel,m}$) in Fig. 7. Since the gas propellent is injected through the anode, the most important contribution to ν in the anodic region is provided by the ν_{e-n} term (collisions between electrons and neutrals). Moving from the anode toward the ionization zone and the channel exit, the anomalous term ν_w rapidly becomes dominant over classical effects (ν_C and ν_{e-n}) due to the progressive decrease of the neutral gas density. The Coulomb collision (ν_C) frequency is at least one order of

magnitude lower than ν_{e-N} inside the channel. Outside the exhaust, ν is almost coincident with the anomalous contribution ν_B. Moreover, as one can notice, ν_B in the near field plume is markedly larger than ν_w for the considered simulation. This is expected since – as previously shown in in [49] for a full-scale SPT-100 Hall thruster – the ratio α/k_B directly influences the plasma conductivity discontinuity across the exhaust that generates the potential drop responsible for the ion acceleration.

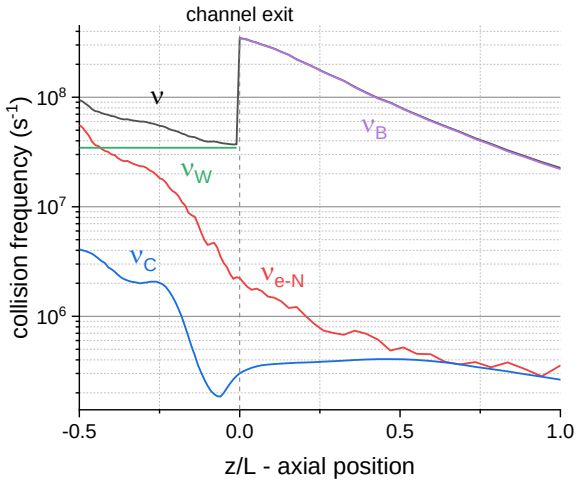

Fig. 7: Terms of the total electron momentum transfer collision frequency (ν, black) for the simulation corresponding to $\varepsilon_{rel,m}$ ($\alpha = 3, k_B = 0.38$, dashed line).

Overall, this parametric study shows that – while providing a useful qualitative description of the thruster behavior – the described simple two-region model for the anomalous electron transport cannot fully reproduce the measured global thruster performance. Indeed – as described above – further increasing the values for the α and k_B parameters above the considered limits to increase the thrust would produce a higher discharge current, further lowering the efficiency. Moreover, as highlighted by other studies on higher power Hall thrusters [67], the hypothesis of a uniform anomalous collision frequency inside the thruster wall partially prevents an accurate representation of the acceleration structure of the thruster. Subsequently, the authors of [67] showed that a significative improvement can be obtained using three-region models. For all the above reasons, a more sophisticated approach with respect to a two-region model is adopted in the following section of this work to describe the collision frequency.

F. Continuous Effective Collision Frequency Profile

In this section, a different approach is applied to model the 50 W-class miniaturized AHT, aiming to overcome the limitations shown by the method described in the previous section. The adopted strategy consists of directly

enforcing a continuous effective electron collision frequency profile along the thruster channel centerline. The goal is to reproduce both the measured global thruster performance and to obtain an acceleration structure consistent with the measurements performed on the laboratory thruster. With reference to Eq. (11), the two terms responsible for anomalous transport inside and outside the channel exit (ν_w, ν_B) are unified into a single one, denoted here onwards as ν_{an}. For the sake of simplicity, ν_{an} is uniform in the radial direction, so that $\nu_{an} = \nu_{an}(z)$, i.e., the enforced anomalous collision frequency depends only on the axial position z.

Starting from the overall best-fitting collision frequency profile obtained with the methodology described in Section 4.2 (simulation marked as $\varepsilon_{rel,m}$), ν_{an} is iteratively changed until reaching a satisfactory agreement with three measured physical quantities. Different algorithmic strategies were attempted but ultimately human-in-the-loop expertise was used to drive the presented "optimal" collision frequency profile. The measured quantities are 1) the discharge current, 2) the most probable velocity of the Xe ions along the channel centerline, and 3) the electric potential. As anticipated in Section 3, LIF spectroscopic measurements of the ion velocity distribution function (IVDF) were performed in [61] in the thruster plume. The electric potential along the channel centerline was also measured in [61], both using LIF and a floating emissive probe, showing a good agreement between the two diagnostics. In this work, the measurements are extended to also capture the electric potential profile inside the thruster channel.

The simulated most probable ion velocity ($v_{i,sim}$) and electric potential (ϕ_{sim}) are compared to the measurement ($v_{i,meas}$ and ϕ_{meas}, respectively) in Fig. 8(a). Note that – as described in Section 4.1.1 – the simulations are performed with a reduced anode voltage, see $V_{anode,sim}$ in Fig. 8(a). Hence, ϕ_{sim} is shifted by $\Delta\phi_{meas}(z_{end})$, i.e., the electric potential measured at $z/L = 1$, corresponding to the downstream end of the computational domain (cathodic magnetic field line).

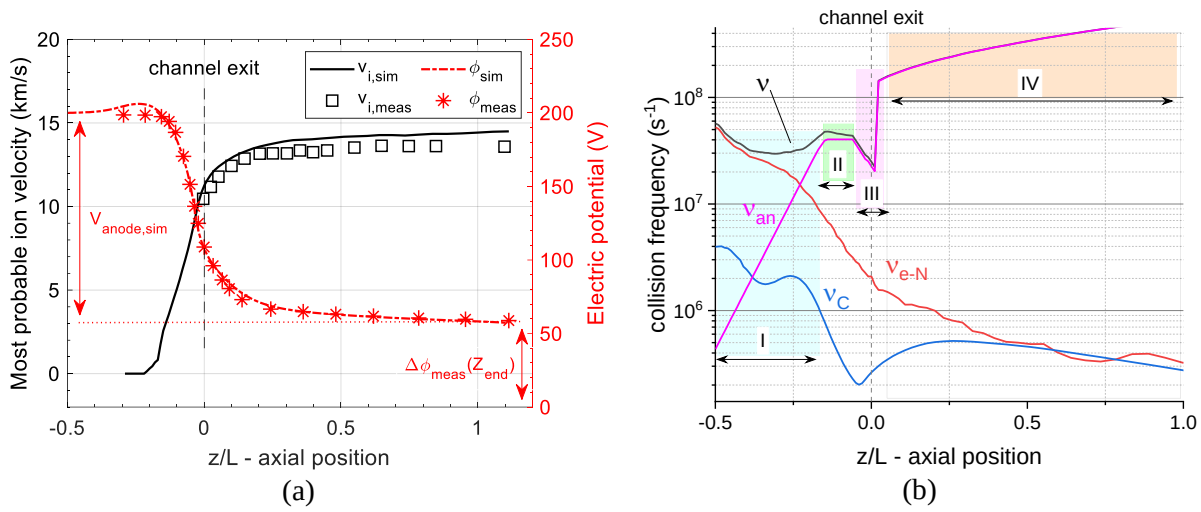

Fig. 8: (a) Most probable ion velocity and electric potential along the channel centerline; (b) corresponding classical (ν_{e-N}, ν_C) and anomalous ($\nu_{an} = \nu_w + \nu_B$) contributions to the electron collision frequency.

The enforced anomalous collision frequency profile ν_{an} is also provided in Fig. 8(b), along with the Coulomb (ν_C) and electron-neutral (ν_{e-N}) contributions to the total (ν) momentum-exchange collision frequency. Coherently with the results shown in Fig. 7, the electron-neutral collisions are markedly dominant over Coulomb collisions inside the channel. Still, ν_{e-N} is the main collisional process only in the anodic zone, with the total frequency being dominated by the anomalous term in the remaining parts of the computational domain. The anomalous collision frequency profile ν_{an} in Fig. 8(b) can be subdivided into four distinct zones. Starting from a rather low value ($4.3 \cdot 10^5$ s^{-1}) at the anode (zone I), ν_{an} is monotonically increased by two orders of magnitude, to reach a constant value of ($4 \cdot 10^7$ s^{-1}) in zone II. The latter value and the extension of zone II have a strong influence on the obtained ion velocity. Lowering ν_{an} in zone II decreases the local plasma conductivity σ. The resulting voltage drop leads to ion velocities higher than those measured. On the other hand, extending zone II toward the anode or further increasing ν_{an} enhances the discharge current I_d. Hence, the trend in zone I serves the twofold purpose of limiting I_d while still providing a sufficient contribution to ν just before zone II. In zone III ν_{an} is lowered to $2 \cdot 10^7$ s^{-1}, and subsequently rapidly increased to $1.2 \cdot 10^8$ s^{-1}. A similar ν_{an} trend – characterized by a sharp discontinuity across the channel exit – was also used in other previous works on different thrusters [48,49,67]. This is needed to ensure that the main part of the ion acceleration takes place across in the exhaust region. Finally, the monotonic increase in the left part of zone IV is necessary to match the measured electric potential shape in the first few millimeters from the channel exit, see ϕ_{meas} in Fig. 8(a). The described profile of ν_{an} can be compared to ν_w and ν_B used for the $\varepsilon_{rel,m}$ case in Section 4.2, Fig. 7. The excess of ν_w inside the channel (especially in the anodic and ionization regions) is responsible for the obtained

low anode effiency η. Furthermore, the lower gradient of σ in the exhaust region contributes to the obtained values for T and Isp being lower than the measurements.

The enforcement of the anomalous collision frequency profile ν_{an} along the channel middle line reproduced the measured ion velocity and electric potential with reasonable accuracy. The global thruster performance yielded by the electron collision frequency profile in Fig. 8(b) are marked as *Simulation – continuous* ν_{an} in Table 1, where they are compared to the experimental measurements and to the two-region model results. The simulated values of thrust, specific impulse, and anode efficiency show a closer agreement with the measurements compared to when the simple two-region model is used to model the anomalous transport.

Doubly Charged Ion Generation

As anticipated, one of the physical peculiarities associated with miniaturized thrusters is the presence of a higher doubly charged ions fraction with respect to full-scale Hall thruster designs. Measurements performed in [61,68] with an $E \times B$ probe have indicated that 10 % of the measured current is due to Xe^{2+} in the considered AHT. Note that similar values have been obtained in [69] for a low-power cylindrical Hall thruster. The rate coefficients for the ionization processes considered in the model are obtained from the integration over a Maxwellian energy distribution function of the corresponding inelastic cross sections. These are taken from [70], [71] and [72] for $Xe \rightarrow Xe^{+}$, $Xe^{+} \rightarrow Xe^{2+}$ and $Xe \rightarrow Xe^{2+}$, respectively. The obtained ionization rate coefficients, shown in Fig. 9, are in good agreement with the previous work of other authors [50,73].

2D maps of the total ionization source term and electric potential obtained when using the collision frequency profile of Fig. 8(b) are shown in Fig. 10(a) and Fig. 10(b). The individual source terms corresponding to the three kinetic channels for the production of ions are shown along the thruster channel centerline in Fig. 10(c) with the electron mean energy ϵ. The maximum of ϵ is located where the radial magnetic field is strongest, see Fig. 10(d) which also shows the number density distribution of Xe, Xe^{+}, Xe^{++} for the same simulation along the channel centerline. For both single and double ions the peak of the source term is displaced toward the inside of the channel with respect to the electron energy maximum, meaning that a satisfactory separation between the acceleration and ionization zone is reached. As expected, the main contribution to the generation of ion species is given by single ions. This is due to the lower threshold energy (12 eV) compared to processes involving double ions (32 eV for $Xe \rightarrow Xe^{2+}$, and 21 eV for $Xe^{+} \rightarrow Xe^{2+}$). With respect to the multiply charged ions, despite a larger threshold energy required to

produce a doubly charged ion from the ground state, the two considered kinetic channels produce a comparable contribution within the thruster channel. This is due to the lower rate coefficient for the double ionization from ground state being compensated by a higher availability of neutrals with respect to Xe^+, required for the stepwise ionization process. However, the stepwise ionization process becomes dominant in the plume. This is due to the electron mean energy and the Xe density decrease shown in Fig. 10(c) and Fig. 10(d), respectively. The simulation described in Section 4.3 yielded a ~9.9 % doubly charged ions contribution to the discharge current. This result is in good agreement with the measured value (10 %). In addition, as pointed out in [74], the presence of a significant population of double ions might also contribute to the anomalous electron transport.

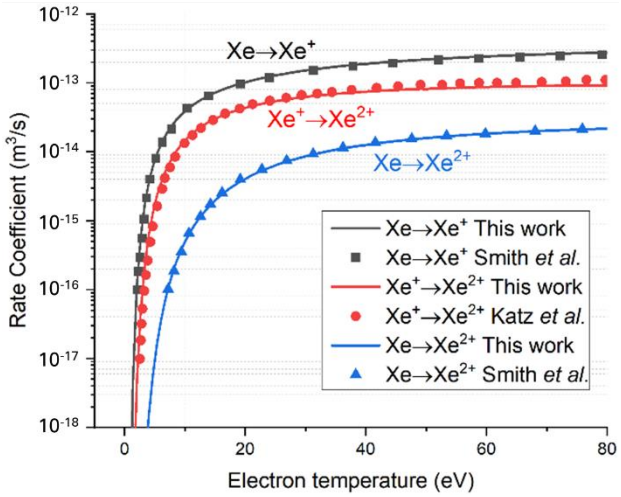

Fig. 9: Rate coefficients for the considered ionization processes, compared to [50,73].

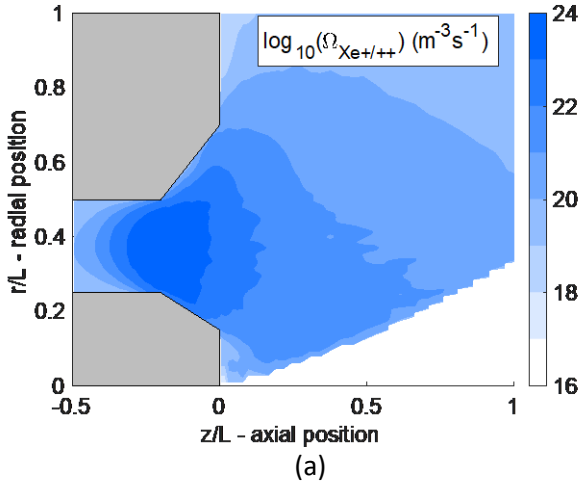

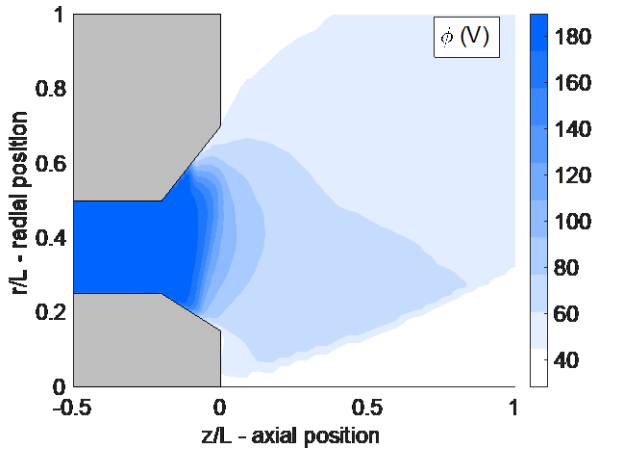

(b)

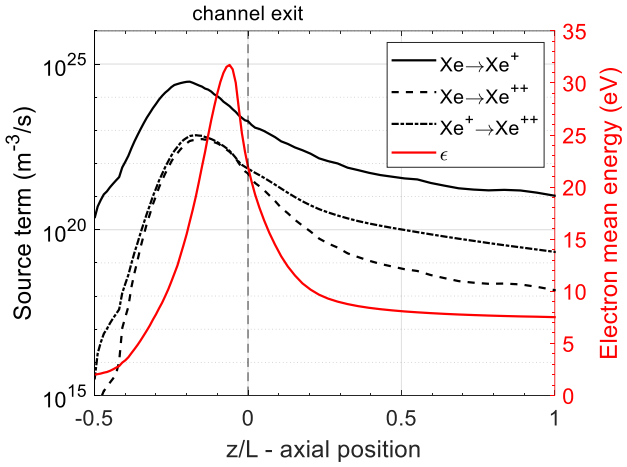

(c)

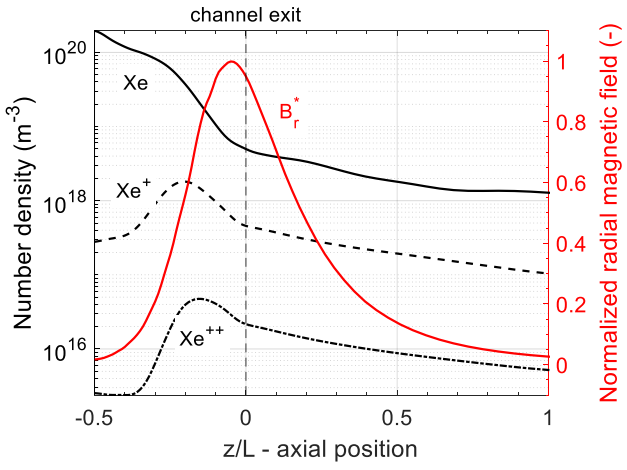

(d)

Fig. 10: (a) Total ionization source term; (b) electric potential; (c) Source terms and mean electron energy and (d) number densities and normalized radial magnetic field along the thruster channel centerline.

Current oscillations

The results in Table 1 show that the model reproduced the measured mean discharge current value thanks to the enforced momentum-exchange collision frequency ν_{an}. Here we compare the simulated and measured current oscillations. Figure 11 (a) shows the measured current amplitude with respect to the mean current value, i.e., the quantity $I_d(t) - \overline{I}_d$, where $\overline{I}_d$ is the average discharge current, over 1 ms. The same physical quantity, obtained from simulations performed with the collision frequency in Fig. 8(b), is shown in Fig. 11 (c). Notably, the results are in good agreement, with both similar amplitudes and temporal distribution of current peaks. The spectra corresponding to the two time-domain profiles are shown in Fig. 11 (b) and (d), respectively. The frequency analysis shows that in both cases the largest spectral component is close to 50 kHz, which can be associated to the periodic depletion of neutrals. We also note that the rather large frequency of these oscillations is also compatible with the limited amplitude.

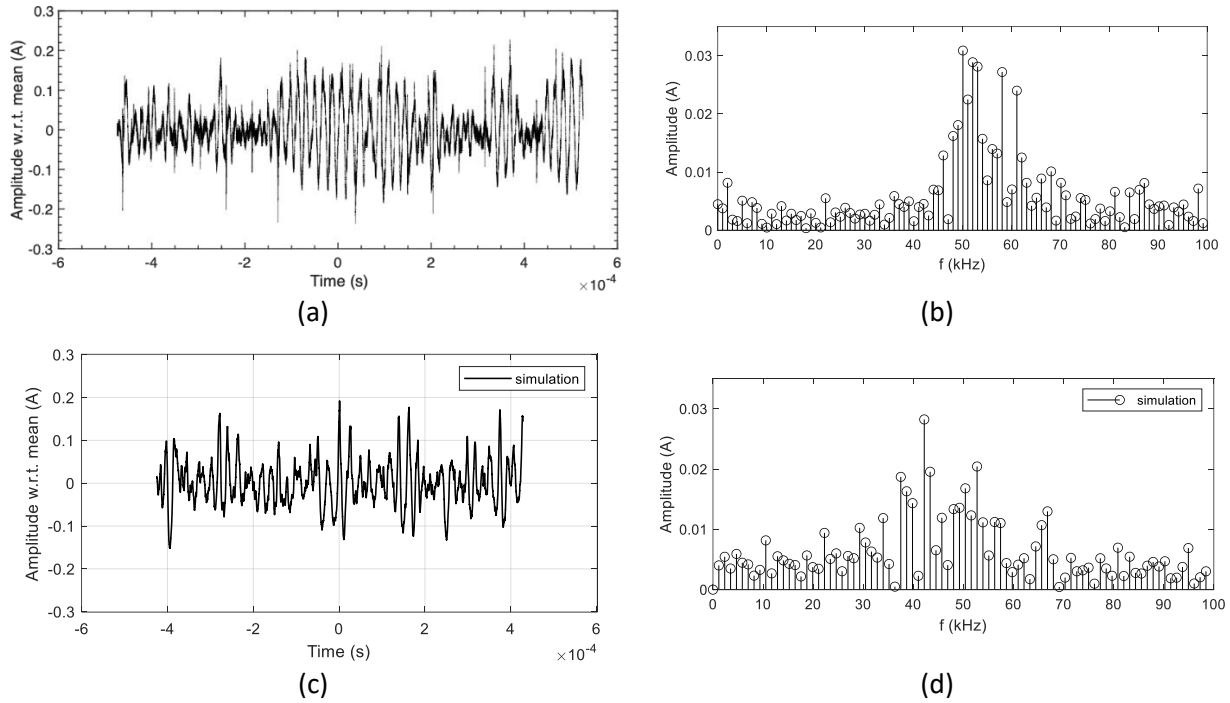

Fig. 11: Measured and simulated discharge current oscillations (amplitude with respect to mean value) and associated spectral components; measurements: (a), (b); simulations: (c), (d).

Ion velocity distribution function

As described in Section 3, the velocity distribution function (VDF) of Xe^+ was measured using LIF spectroscopy along the channel middle line. The measured VDF is shown in Fig. 12 (a) (black dotted line) for increasing values of

z, i.e., the distance from the thruster exit plane. A tail of ions slower than the main beam (magenta circle) is consistently observed for all the considered values of z. Furthermore, starting from $z = 3$ mm, a low-velocity secondary peak is observed (orange rectangle). The magnitude of the peak increases with increasing values of z. In the same figure, the measured IVDF is compared with the results of three simulations. The results marked as $\epsilon_c = 7.5$ eV correspond to the simulation described in Section 4.3, with the electron anomalous collision frequency shown in Fig. 8(a). The simulated IVDF has a markedly narrower full width at half maximum (FWHM) and does not exhibit the measured slower ion tail (magenta). However, the simulation shows a similar (qualitative) trend for the low-velocity secondary peak (orange). In [75] the authors argue that the slow ion population that they measured in the near-field plume of an SPT-100 thruster along the discharge channel centerline might be due to CEX collision between ions and neutrals. The results marked as $\epsilon_c = 7.5$ eV w/o CEX are obtained from a simulation with the same settings as the previous one, with the only exception of CEX collisions, which are disregarded for the sake of comparison. The results show that – while CEX events influence the slow ions, this phenomenon can hardly be the only cause for the densely populated slow groups obtained from the measurements. Still, as pointed out in [76], CEX could also play an additional role in when measurements are performed with RPAs, since Xe ions might interact with surfaces inside the RPA. However, in our work the IVDF was measured through laser-induced fluorescence, which is not affected by this issue, ruling out this possible source of uncertainty.

Several authors including [75] have observed experimentally that a higher availability of neutrals in the near-field plume is correlated with the discussed appearance of slow ion groups, especially when populations of energetic electrons are present. As expected, increasing the background pressure by a factor of 10 yielded a noticeably more populated low velocity tail of ions in our simulations, see Fig. 12 (b).

We note that a marked increase in the slow ion population is obtained if higher electron mean energies are considered. This is shown in Fig. 12 (a) by setting the cathodic boundary condition for ϵ_c to 15 eV. Increasing the electron mean energy at the cathodic line causes significant changes of ϵ only in the plume, and not inside the thruster channel. This means that the same is valid for the singly and doubly charged ions source terms. Consequently, the thruster performance and the dynamics of the fast ions are not significantly altered by boundary conditions changes. The observed generation of a secondary peak of slow ions in the measured IVDF could be correlated with the presence of energetic electrons in the near-field plume, whose dynamics cannot be fully captured in our model because of the assumption of Maxwellian electron energy distribution function (EEDF). In fact, experimental measurements

performed on small-scale thrusters with similar anode voltage levels have highlighted the presence of a non-Maxwellian EEDF outside the thruster channel [77,78]. The observed EEDF is characterized by a high-energy electron population, superimposed on the low energy bulk, and has been attributed to hollow cathode operation [78].

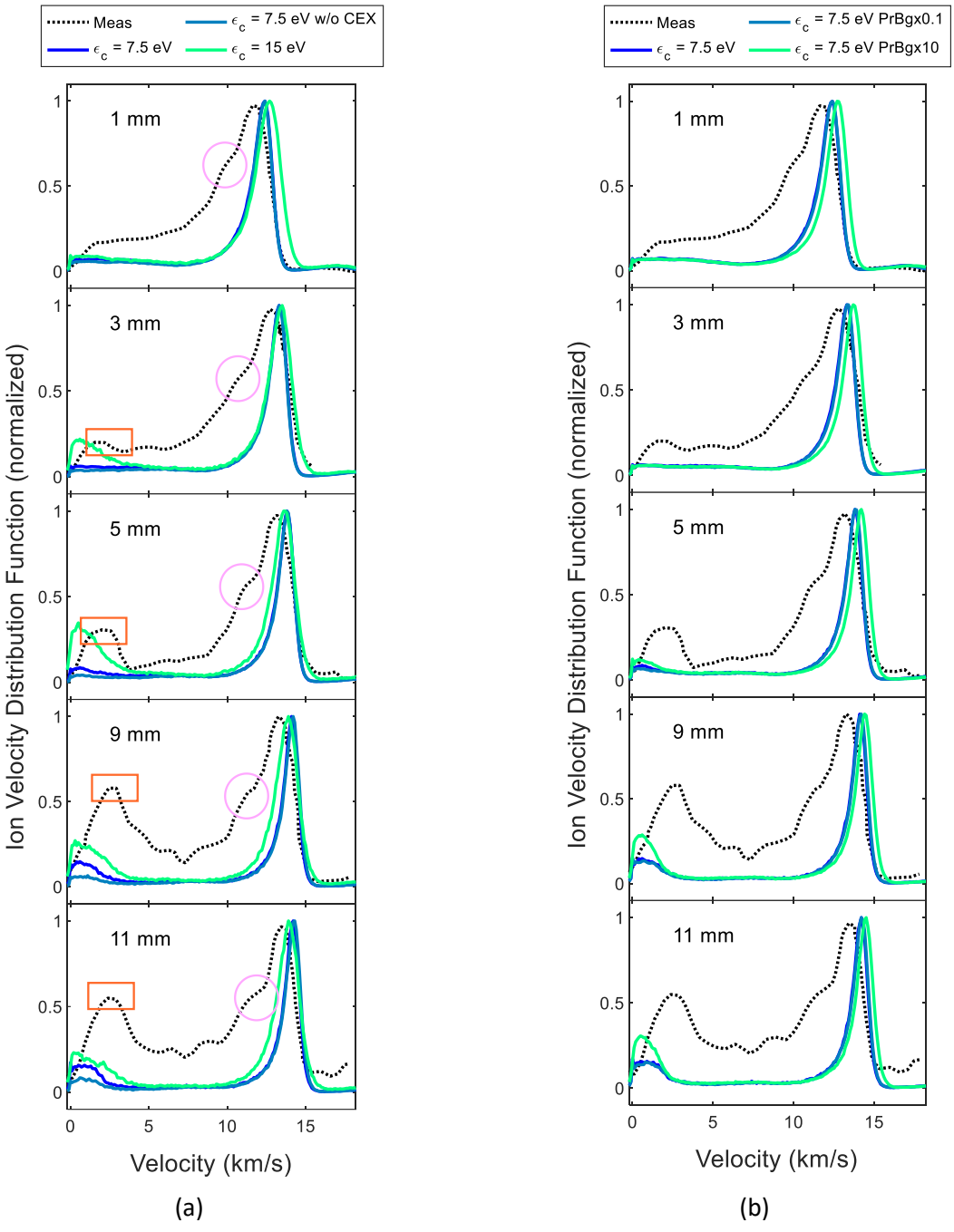

Fig. 12: Measured and computed IVDF for increasing distances from channel end; (a) influence of boundary conditions for ϵ and CEX collisions; (b) influence of background pressure.

V.Conclusion

In this work, a hybrid fluid/particle-in-cell code has been employed to study a miniaturized 50 W-class Hall thruster for space propulsion. The analysis was carried out by comparing results yielded by two different treatments of the anomalous electron transport with experimental measurements. In particular, the physical information provided by LIF measurements of the most probable ion velocity and electrostatic potential has been used to infer the anomalous contributions to the cross-field electron transport, subsequently enforced in the employed electron-fluid model. The study highlights that – in the context of modeling this kind of devices with non-self-consistent methodologies, i.e., that rely on empirical expressions for the anomalous electron transport – the macroscopic information provided by measurements of the global thruster performance is not fully sufficient to provide an exhaustive representation of the detailed physics involved in such devices. We have discussed the effects of the cathode on the local plasma potential and have shown a methodology to correct the computed thruster performance accordingly. Overall, due to the microscopic information provided by LIF and emissive probe measurements, the enforcement of a continuous anomalous collision frequency allowed to reproduce several features of the acceleration structure of the considered Hall thruster, as well as the discharge current oscillations and the ratio between singly and doubly charged Xe ions. The respective efficiency of the two kinetic channels (double ionization from the ground state and stepwise ionization) for the production of doubly charged ions has been discussed and correlated with the computed spatial distribution of the species. Finally, the computed ion velocity distribution has been compared to experimental measurements and we speculated the presence of energetic electrons, which are probably correlated with the hollow cathode keeper voltage required for stable operation of the thruster.

Funding Sources

The authors want to thank the Partnership Hubert Curien (PHC) Star Program between France and Republic of Korea. The authors also want to thank the Science and Technology Amicable Relationships (STAR) Program (Grant No. NRF-2019K1A3A1A21031236) via the National Research Foundation of Korea, funded by the Ministry of Science and ICT, Republic of Korea.

References

[1] Jahn, R. G., “Physics of Electric Propulsion,” McGraw-Hill, New York, 1968.
[2] Goebel, D. M., and Katz, I., “Fundamentals of Electric Propulsion: Ion and Hall Thrusters,” John Wiley & Sons,

Inc., Hoboken, NJ, 2008.
[3] Ahedo, E., "Plasmas for Space Propulsion," *Plasma Physics and Controlled Fusion*, Vol. 53, No. 12, 2011, p. 124037. https://doi.org/10.1088/0741-3335/53/12/124037
[4] Charles, C., "Plasmas for Spacecraft Propulsion," *Journal of Physics D: Applied Physics*, Vol. 42, No. 16, 2009, p. 163001. https://doi.org/10.1088/0022-3727/42/16/163001
[5] Lev, D., Myers, R. M., Lemmer, K. M., Kolbeck, J., Koizumi, H., and Polzin, K., "The Technological and Commercial Expansion of Electric Propulsion," *Acta Astronautica*, Vol. 159, 2019, pp. 213–227. https://doi.org/10.1016/j.actaastro.2019.03.058
[6] Mazouffre, S., "Electric Propulsion for Satellites and Spacecraft: Established Technologies and Novel Approaches," *Plasma Sources Science and Technology*, Vol. 25, No. 3, 2016, p. 033002. https://doi.org/10.1088/0963-0252/25/3/033002
[7] Keidar, M., Zhuang, T., Shashurin, A., Teel, G., Chiu, D., Lukas, J., Haque, S., and Brieda, L., "Electric Propulsion for Small Satellites," *Plasma Physics and Controlled Fusion*, Vol. 57, No. 1, 2014, p. 014005. https://doi.org/10.1088/0741-3335/57/1/014005
[8] Mazouffre, S., and Grimaud, L., "Characteristics and Performances of a 100-W Hall Thruster for Microspacecraft," *IEEE Transactions on Plasma Science*, Vol. 46, No. 2, 2018, pp. 330–337. https://doi.org/10.1109/TPS.2017.2786402
[9] Conversano, R. W., Goebel, D. M., Hofer, R. R., Matlock, T. S., and Wirz, R. E., "Development and Initial Testing of a Magnetically Shielded Miniature Hall Thruster," *IEEE Transactions on Plasma Science*, Vol. 43, No. 1, 2015, pp. 103–117. https://doi.org/10.1109/TPS.2014.2321107
[10] Brown, N. P., and Walker, M. L. R., "Review of Plasma-Induced Hall Thruster Erosion," *Applied Sciences*, Vol. 10, No. 11, 2020, p. 3775. https://doi.org/10.3390/app10113775
[11] Mikellides, I. G., and Katz, I., "Numerical Simulations of Hall-Effect Plasma Accelerators on a Magnetic-Field-Aligned Mesh," *Physical Review E*, Vol. 86, No. 4, 2012, p. 046703. https://doi.org/10.1103/PhysRevE.86.046703
[12] Andreussi, T., Giannetti, V., Leporini, A., Saravia, M. M., and Andrenucci, M., "Influence of the Magnetic Field Configuration on the Plasma Flow in Hall Thrusters," *Plasma Physics and Controlled Fusion*, Vol. 60, No. 1, 2017, p. 014015. https://doi.org/10.1088/1361-6587/aa8c4d
[13] Keidar, M., Boyd, I. D., and Beilis, I. I., "Modeling of a High-Power Thruster with Anode Layer," *Physics of Plasmas*, Vol. 11, No. 4, 2004, pp. 1715–1722. https://doi.org/10.1063/1.1668642
[14] Merino, M., Cichocki, F., and Ahedo, E., "A Collisionless Plasma Thruster Plume Expansion Model," *Plasma Sources Science and Technology*, Vol. 24, No. 3, 2015, p. 035006. https://doi.org/10.1088/0963-0252/24/3/035006
[15] Li, N., Liu, Y., Liu, C., and Wu, M., "An Integrated Fluid Simulation Platform on Hall Thruster Plasmas," *AIP Advances*, Vol. 12, No. 1, 2022, p. 015117. https://doi.org/10.1063/5.0078222
[16] Ortega, A. L., Mikellides, I. G., Chaplin, V. H., Snyder, J. S., and Lenguito, G., "Facility Pressure Effects on a Hall Thruster with an External Cathode: I. Numerical Simulations," *Plasma Sources Science and Technology*, Vol. 29, No. 3, 2020, p. 035011. https://doi.org/10.1088/1361-6595/ab6c7e
[17] Mikellides, I. G., Ortega, A. L., Chaplin, V. H., and Snyder, J. S., "Facility Pressure Effects on a Hall Thruster with an External Cathode, II: Theoretical Model of the Thrust and the Significance of Azimuthal Asymmetries in the Cathode Plasma," *Plasma Sources Science and Technology*, Vol. 29, No. 3, 2020, p. 035010. https://doi.org/10.1088/1361-6595/ab6c7f
[18] "Full Fluid Moment Model for Low Temperature Magnetized Plasmas | Physics of Plasmas | AIP Publishing." Retrieved 16 February 2024. https://pubs.aip.org/aip/pop/article/27/11/113505/107939/Full-fluid-moment-model-for-low-temperature
[19] Wang, L., Hakim, A., Juno, J., and Srinivasan, B., "Electron Cyclotron Drift Instability and Anomalous Transport: Two-Fluid Moment Theory and Modeling," *Plasma Sources Science and Technology*, Vol. 31, No. 10, 2022, p. 105001. https://doi.org/10.1088/1361-6595/ac90e7
[20] Boccelli, S., McDonald, J. G., and Magin, T. E., "14-Moment Maximum-Entropy Modeling of Collisionless Ions for Hall Thruster Discharges," *Physics of Plasmas*, Vol. 29, No. 8, 2022, p. 083903. https://doi.org/10.1063/5.0100092
[21] Raisanen, A. L., Hara, K., and Boyd, I. D., "Two-Dimensional Hybrid-Direct Kinetic Simulation of a Hall Thruster Discharge Plasma," *Physics of Plasmas*, Vol. 26, No. 12, 2019. https://doi.org/10.1063/1.5122290
[22] Chan, W. H. R., and Boyd, I. D., "Grid-Point Requirements for Direct Kinetic Simulation of Weakly Collisional Plasma Plume Expansion," *Journal of Computational Physics*, Vol. 475, 2023. https://doi.org/10.1016/j.jcp.2022.111861
[23] Taccogna, F., Schneider, R., Longo, S., and Capitelli, M., "Kinetic Simulations of a Plasma Thruster," *Plasma Sources Science and Technology*, Vol. 17, No. 2, 2008, p. 024003. https://doi.org/10.1088/0963-0252/17/2/024003

[24] Lafleur, T., Baalrud, S. D., and Chabert, P., "Theory for the Anomalous Electron Transport in Hall Effect Thrusters. II. Kinetic Model," *Physics of Plasmas*, Vol. 23, No. 5, 2016, p. 053503. https://doi.org/10.1063/1.4948496
[25] Taccogna, F., and Minelli, P., "Three-Dimensional Particle-in-Cell Model of Hall Thruster: The Discharge Channel," *Physics of Plasmas*, Vol. 25, No. 6, 2018, p. 061208. https://doi.org/10.1063/1.5023482
[26] Tejeda, J. M., Reza, M., Faraji, F., and Knoll, A., "Performance Enhancement of Hall Effect Thrusters Using Radiofrequency Excitation," *Acta Astronautica*, Vol. 194, 2022, pp. 145–161. https://doi.org/10.1016/j.actaastro.2022.01.033
[27] Deluzet, F., Fubiani, G., Garrigues, L., Guillet, C., and Narski, J., "Sparse Grid Reconstructions for Particle-In-Cell Methods," *ESAIM: Mathematical Modelling and Numerical Analysis*, Vol. 56, No. 5, 2022, pp. 1809–1841. https://doi.org/10.1051/m2an/2022055
[28] Reza, M., Faraji, F., and Knoll, A., "Resolving Multi-Dimensional Plasma Phenomena in Hall Thrusters Using the Reduced-Order Particle-in-Cell Scheme," *Journal of Electric Propulsion*, Vol. 1, No. 1, 2022, p. 19. https://doi.org/10.1007/s44205-022-00019-6
[29] Boeuf, J. P., and Garrigues, L., "Low Frequency Oscillations in a Stationary Plasma Thruster," *Journal of Applied Physics*, Vol. 84, No. 7, 1998, pp. 3541–3554. https://doi.org/10.1063/1.368529
[30] Komurasaki, K., and Arakawa, Y., "Two-Dimensional Numerical Model of Plasma Flow in a Hall Thruster," *Journal of Propulsion and Power*, Vol. 11, No. 6, 1995, pp. 1317–1323. https://doi.org/10.2514/3.23974
[31] Fife, J. M., "Hybrid-PIC Modeling and Electrostatic Probe Survey of Hall Thrusters," PhD Thesis. Massachusetts Institute of Technology, 1998.
[32] Kawashima, R., Hara, K., and Komurasaki, K., "Numerical Analysis of Azimuthal Rotating Spokes in a Crossed-Field Discharge Plasma," *Plasma Sources Science and Technology*, Vol. 27, No. 3, 2018, p. 035010. https://doi.org/10.1088/1361-6595/aab39c
[33] Lam, C. M., Fernandez, E., and Cappelli, M. A., "A 2-D Hybrid Hall Thruster Simulation That Resolves the ExB Electron Drift Direction," *IEEE Transactions on Plasma Science*, Vol. 43, No. 1, 2015, pp. 86–94. https://doi.org/10.1109/TPS.2014.2356650
[34] Koo, J. W., and Boyd, I. D., "Computational Model of a Hall Thruster," *Computer Physics Communications*, Vol. 164, No. 1, 2004, pp. 442–447. https://doi.org/10.1016/j.cpc.2004.06.058
[35] Morozov, A. I., and Savel'ev, V. V., "One-Dimensional Hybrid Model of a Stationary Plasma Thruster," *Plasma Physics Reports*, Vol. 26, No. 10, 2000, pp. 875–880. https://doi.org/10.1134/1.1316827
[36] Ahedo, E., "Presheath/Sheath Model with Secondary Electron Emission from Two Parallel Walls," *Physics of Plasmas*, Vol. 9, No. 10, 2002, pp. 4340–4347. https://doi.org/10.1063/1.1503798
[37] Sommier, E., Scharfe, M. K., Gascon, N., Cappelli, M. A., and Fernandez, E., "Simulating Plasma-Induced Hall Thruster Wall Erosion With a Two-Dimensional Hybrid Model," *IEEE Transactions on Plasma Science*, Vol. 35, No. 5, 2007, pp. 1379–1387. https://doi.org/10.1109/TPS.2007.905943
[38] Mikellides, I. G., Katz, I., Hofer, R. R., Goebel, D. M., Grys, K. de, and Mathers, A., "Magnetic Shielding of the Channel Walls in a Hall Plasma Accelerator," *Physics of Plasmas*, Vol. 18, No. 3, 2011, p. 033501. https://doi.org/10.1063/1.3551583
[39] Mikellides, I. G., and Ortega, A. L., "Challenges in the Development and Verification of First-Principles Models in Hall-Effect Thruster Simulations That Are Based on Anomalous Resistivity and Generalized Ohm's Law*," *Plasma Sources Science and Technology*, Vol. 28, No. 1, 2019, p. 014003. https://doi.org/10.1088/1361-6595/aae63b
[40] Lafleur, T., Baalrud, S. D., and Chabert, P., "Theory for the Anomalous Electron Transport in Hall Effect Thrusters. I. Insights from Particle-in-Cell Simulations," *Physics of Plasmas*, Vol. 23, No. 5, 2016, p. 053502. https://doi.org/10.1063/1.4948495
[41] Brown, Z., Dale, E., and Jorns, B., "Experimental Correlation between Anomalous Electron Collision Frequency and Plasma Turbulence in a Hall Effect Thruster," presented at the IEPC-2019-843, 2019.
[42] Taccogna, F., and Garrigues, L., "Latest Progress in Hall Thrusters Plasma Modelling," *Reviews of Modern Plasma Physics*, Vol. 3, No. 1, 2019, p. 12.
[43] Jung, G., and Sung, H.-G., "A Study on Particle Collisions in Hall Thruster Plasma Using a Hybrid PIC-DSMC Model," *International Journal of Aeronautical and Space Sciences*, Vol. 23, No. 2, 2022, pp. 326–338. https://doi.org/10.1007/s42405-021-00435-2
[44] Shashkov, A., Tyushev, M., Lovtsov, A., Tomilin, D., and Kravchenko, D., "Machine Learning-Based Method to Adjust Electron Anomalous Conductivity Profile to Experimentally Measured Operating Parameters of Hall Thruster," *Plasma Science and Technology*, Vol. 24, No. 6, 2022. https://doi.org/10.1088/2058-6272/ac59e1
[45] Shashkov, A., Lovtsov, A., Tomilin, D., and Kravchenko, D., "Numerical Study of Viscosity and Heat Flux Role in Heavy Species Dynamics in Hall Thruster Discharge," *Plasma Science and Technology*, Vol. 25, No. 1, 2022, p. 015511. https://doi.org/10.1088/2058-6272/ac82e0

[46] Panelli, M., Morfei, D., Milo, B., D'aniello, F., and Battista, F., "Axisymmetric Hybrid Plasma Model for Hall Effect Thrusters," *Particles*, Vol. 4, 2021, pp. 296–324. https://doi.org/10.3390/particles4020026
[47] Parra, F. I., Ahedo, E., Fife, J. M., and Martínez-Sánchez, M., "A Two-Dimensional Hybrid Model of the Hall Thruster Discharge," *Journal of Applied Physics*, Vol. 100, No. 2, 2006, p. 023304. https://doi.org/10.1063/1.2219165
[48] Hagelaar, G. J. M., Bareilles, J., Garrigues, L., and Boeuf, J.-P., "Two-Dimensional Model of a Stationary Plasma Thruster," *Journal of Applied Physics*, Vol. 91, No. 9, 2002, pp. 5592–5598. https://doi.org/10.1063/1.1465125
[49] Bareilles, J., Hagelaar, G. J. M., Garrigues, L., Boniface, C., Boeuf, J. P., and Gascon, N., "Critical Assessment of a Two-Dimensional Hybrid Hall Thruster Model: Comparisons with Experiments," *Physics of Plasmas*, Vol. 11, No. 6, 2004, pp. 3035–3046. https://doi.org/10.1063/1.1719022
[50] Smith, B. D., Boyd, I. D., and Kamhawi, H., "Influence of Triply-Charged Ions and Ionization Cross-Sections in a Hybrid-PIC Model of a Hall Thruster Discharge," presented at the AIAA 2014-3429, 2014.
[51] Hara, K., "An Overview of Discharge Plasma Modeling for Hall Effect Thrusters," *Plasma Sources Science and Technology*, Vol. 28, No. 4, 2019, p. 044001. https://doi.org/10.1088/1361-6595/ab0f70
[52] Garrigues, L., "Ion Properties in a Hall Current Thruster Operating at High Voltage," *Journal of Applied Physics*, Vol. 119, No. 16, 2016, p. 163305. https://doi.org/10.1063/1.4947523
[53] Meeker, D., "Finite Element Method Magnetics: User's Manual, Version 4.2," Apr 21 2019.
[54] Chen, F., "Diffusion and Resistivity," *Introduction to Plasma Physics and Controlled Fusion*, Springer International Publishing, Cham, 2016, pp. 145–185. https://doi.org/10.1007/978-3-319-22309-4_5
[55] Morozov, A., "Conditions for Efficient Current Transport by Near-Wall Conduction," *Soviet Journal of Plasma Physics*, Vol. 32, No. 8, 1987, pp. 901–904.
[56] Bugrova, A., "Experimental Investigation of near Wall Conductivity," *Soviet Journal of Plasma Physics*, Vol. 16, 1990, pp. 849–856.
[57] Morozov, A., "Steady-State Uniform Debye Sheaths," *Soviet Journal of Plasma Physics (English Translation)*, Vol. 17, No. 6, 1991, pp. 393–397.
[58] Garrigues, L., Hagelaar, G., Boniface, C., and Boeuf, J., "Anomalous Conductivity and Secondary Electron Emission in Hall Effect Thrusters," *Journal of applied physics*, Vol. 100, No. 12, 2006, p. 123301.
[59] Barral, S., Makowski, K., Peradzyński, Z., Gascon, N., and Dudeck, M., "Wall Material Effects in Stationary Plasma Thrusters. II. Near-Wall and in-Wall Conductivity," *Physics of Plasmas*, Vol. 10, No. 10, 2003, pp. 4137–4152. https://doi.org/10.1063/1.1611881
[60] Ahedo, E., Santos, R., and Parra, F. I., "Fulfillment of the Kinetic Bohm Criterion in a Quasineutral Particle-in-Cell Model," *Physics of Plasmas*, Vol. 17, No. 7, 2010, p. 073507. https://doi.org/10.1063/1.3456516
[61] Lee, D., Doh, G., Kim, H., Garrigues, L., and Choe, W., "Distinct Discharge Modes in Micro Hall Thruster Plasmas," *Plasma Sources Science and Technology*, Vol. 30, No. 3, 2020, p. 035004. https://doi.org/10.1088/1361-6595/abdf19
[62] Doh, G., Park, J., Lee, D., Kim, H., and Choe, W., "Determination of the Ionization Region in Hall Thruster Plasmas with Low Perturbation," *Journal of Applied Physics*, Vol. 130, No. 19, 2021, p. 193301. https://doi.org/10.1063/5.0066974
[63] Doh, G., Kim, H., Lee, D., Park, S., Mazouffre, S., and Choe, W., "Structure of the Ion Acceleration Region in Cylindrical Hall Thruster Plasmas," *Journal of Physics D: Applied Physics*, Vol. 55, No. 22, 2022, p. 225204. https://doi.org/10.1088/1361-6463/ac5773
[64] Lev, D. R., Mikellides, I. G., Pedrini, D., Goebel, D. M., Jorns, B. A., and McDonald, M. S., "Recent Progress in Research and Development of Hollow Cathodes for Electric Propulsion," *Reviews of Modern Plasma Physics*, Vol. 3, No. 1, 2019, p. 6. https://doi.org/10.1007/s41614-019-0026-0
[65] Levchenko, I., Bazaka, K., Ding, Y., Raitses, Y., Mazouffre, S., Henning, T., Klar, P. J., Shinohara, S., Schein, J., Garrigues, L., Kim, M., Lev, D., Taccogna, F., Boswell, R. W., Charles, C., Koizumi, H., Shen, Y., Scharlemann, C., Keidar, M., and Xu, S., "Space Micropropulsion Systems for Cubesats and Small Satellites: From Proximate Targets to Furthermost Frontiers," *Applied Physics Reviews*, Vol. 5, No. 1, 2018, p. 011104. https://doi.org/10.1063/1.5007734
[66] Goebel, D. M., Becatti, G., Mikellides, I. G., and Lopez Ortega, A., "Plasma Hollow Cathodes," *Journal of Applied Physics*, Vol. 130, No. 5, 2021, p. 050902. https://doi.org/10.1063/5.0051228
[67] Hofer, R., Katz, I., Goebel, D., Jameson, K., Sullivan, R., Johnson, L., and Mikellides, I., "Efficacy of Electron Mobility Models in Hybrid-PIC Hall Thruster Simulations," presented at the AIAA 2008-4924, 2008. https://doi.org/10.2514/6.2008-4924
[68] Kim, H., Lim, Y., Choe, W., and Seon, J., "Effect of Multiply Charged Ions on the Performance and Beam Characteristics in Annular and Cylindrical Type Hall Thruster Plasmas," *Applied Physics Letters*, Vol. 105, No. 14,

2014, p. 144104. https://doi.org/10.1063/1.4897948
[69] Garrigues, L., Hagelaar, G. J. M., Boeuf, J. P., Raitses, Y., Smirnov, A., and Fisch, N. J., "Simulations of a Miniaturized Cylindrical Hall Thruster," *IEEE Transactions on Plasma Science*, Vol. 36, No. 5, 2008, pp. 2034–2042. https://doi.org/10.1109/TPS.2008.2003976
[70] Puech, V., and Mizzi, S., "Collision Cross Sections and Transport Parameters in Neon and Xenon," *Journal of Physics D: Applied Physics*, Vol. 24, No. 11, 1991, pp. 1974–1985. https://doi.org/10.1088/0022-3727/24/11/011
[71] Achenbach, C., Muller, A., Salzborn, E., and Becker, R., "Single Ionisation of Multiply Charged Xenon Ions by Electron Impact," *Journal of Physics B: Atomic and Molecular Physics*, Vol. 17, No. 7, 1984, pp. 1405–1425. https://doi.org/10.1088/0022-3700/17/7/023
[72] Wetzel, R. C., Baiocchi, F. A., Hayes, T. R., and Freund, R. S., "Absolute Cross Sections for Electron-Impact Ionization of the Rare-Gas Atoms by the Fast-Neutral-Beam Method," *Physical Review A*, Vol. 35, No. 2, 1987, pp. 559–577. https://doi.org/10.1103/PhysRevA.35.559
[73] Katz, I., Hofer, R. R., and Goebel, D. M., "Ion Current in Hall Thrusters," *IEEE Transactions on Plasma Science*, Vol. 36, No. 5, 2008, pp. 2015–2024. https://doi.org/10.1109/TPS.2008.2004219
[74] Hara, K., and Tsikata, S., "Cross-Field Electron Diffusion Due to the Coupling of Drift-Driven Microinstabilities," *Physical Review E*, Vol. 102, No. 2, 2020, p. 023202. https://doi.org/10.1103/PhysRevE.102.023202
[75] MacDonald-Tenenbaum, N., Pratt, Q., Nakles, M., Pilgram, N., Holmes, M., and Hargus, W., "Background Pressure Effects on Ion Velocity Distributions in an SPT-100 Hall Thruster," *Journal of Propulsion and Power*, Vol. 35, No. 2, 2019, pp. 403–412. https://doi.org/10.2514/1.B37133
[76] Sullivan, R. M., "The Physics of High-Velocity Ions in the Hall Thruster near-Field," phd. California Institute of Technology, 2010.
[77] Fedotov, V. Yu., Ivanov, A. A., Guerrini, G., Vesselovzorov, A. N., and Bacal, M., "On the Electron Energy Distribution Function in a Hall-Type Thruster," *Physics of Plasmas*, Vol. 6, No. 11, 1999, pp. 4360–4365. https://doi.org/10.1063/1.873700
[78] Tichý, M., Pétin, A., Kudrna, P., Horký, M., and Mazouffre, S., "Electron Energy Distribution Function in a Low-Power Hall Thruster Discharge and near-Field Plume," *Physics of Plasmas*, Vol. 25, No. 6, 2018, p. 061205. https://doi.org/10.1063/1.5017578